Received: 16 August 2022 | Revised: 25 November 2022 | Accepted: 29 December 2022

DOI: 10.1111/jace.18986

Journal of the American Ceramic Society

RESEARCH ARTICLE

Phase stability and tensorial thermal expansion properties of single to high-entropy rare-earth disilicates

Alejandro Salanova[1] | **Ian A. Brummel**[1] | **Andrey A. Yakovenko**[2] | **Elizabeth J. Opila**[1] | **Jon F. Ihlefeld**[1,3]

[1]Department of Materials Science and Engineering, University of Virginia, Charlottesville, Virginia, USA

[2]Advanced Photon Source, Argonne National Laboratory, Lemont, Illinois, USA

[3]Charles L. Brown Department of Electrical and Computer Engineering, University of Virginia, Charlottesville, Virginia, USA

Correspondence
Alejandro Salanova and Jon F. Ihlefeld, Department of Materials Science and Engineering, University of Virginia, Charlottesville, VA 22904, USA.
Email: as2ej@virginia.edu; jihlefeld@virginia.edu

Funding information
U.S. National Science Foundation's (NSF) Designing Materials to Revolution and Engineer our Future (DMREF) Program, Grant/Award Number: 1921973

Abstract

Temperature limitations in nickel-base superalloys have resulted in the emergence of SiC-based ceramic matrix composites as a viable replacement for gas turbine components in aviation applications. Higher operating temperatures allow for reduced fuel consumption but present a materials design challenge related to environmental degradation. Rare-earth disilicates ($RE_2Si_2O_7$) have been identified as coatings that can function as environmental barriers and minimize hot component degradation. In this work, single- and multiple-component rare-earth disilicate powders were synthesized via a sol-gel method with compositions selected to exist in the monoclinic $C\,2/m$ phase (β phase). Phase stability in multiple cation compositions was shown to follow a rule of mixtures and the $C\,2/m$ phase could be realized for compositions that contained up to 25% dysprosium, which typically only exists in a triclinic, $P\,\bar{1}$, phase. All compositions exhibited phase stability from room temperature to 1200°C as assessed by X-ray diffraction. The thermal expansion tensors for each composition were determined from high-temperature synchrotron X-ray diffraction and accompanying Rietveld refinements. It was observed that ytterbium-containing compositions had larger changes in the α_{31} shear component with increasing temperature that led to a rotation of the principal axes. Principal axes rotation of up to 47° were observed for ytterbium disilicate. The results suggest that microstructure design and crystallographic texture may be essential future avenues of investigation to ensure thermo-mechanical robustness of rare-earth disilicate environmental barrier coatings.

KEYWORDS
anisotropy, environmental barrier coatings (EBC), sol-gel, thermal expansion

1 | INTRODUCTION

Nickel-base superalloys have reached the limit of their high temperature capabilities within gas turbine engines. Silicon carbide-based ceramic matrix composites (CMCs) provide a stronger, lighter, and more durable alternative to Ni-base turbine blades and vanes.[1–4] In a combustion environment, however, SiC reacts with water vapor to form a

gaseous silicon hydroxide species.[5] This volatilization reaction is shown in Equation 1 and can be minimized through the application of thermal/environmental barrier coatings (T/EBCs).[1,6–11]

$$SiO_2(s) + 2H_2O(g) = Si(OH)_4(g) \quad (1)$$

Rare earth disilicates (REDS) have been identified as promising T/EBC candidates due to their combination of a low coefficient of thermal expansion (CTE) mismatch with CMCs, high melting temperatures, and a low silicon activity relative to pure silicon oxide.[12] In application, however, REDS still undergo reactions with water vapor and can transform into a rare-earth monosilicate or rare-earth oxide. One possible mechanism to increase the thermodynamic stability of REDS coatings is through the inclusion of multiple rare earth (RE) cations in equimolar ratios. With every cation addition, the configurational entropy increases and compositions containing five equimolar cations in solid solution are known as high-entropy (HE) ceramics.[13,14] High entropy ceramics may have their free energy reduced compared to their individual components due to the negative $T\Delta S$ portion of Gibbs free energy and high configurational entropy and the addition of multiple REs can result in local ion mass variations and distortions within the lattice that serve to reduce phonon mean free paths. A reduction in phonon mean free path leads to a reduction in thermal conductivity,[15,16] which makes the HE approach attractive for T/EBCs in ways single component REDS cannot.

Creating high entropy REDS requires consideration of cation size dependence of phase stability. When multiple cations are added into solid solution, the final phase is hypothesized to follow a rule of mixtures. Within the REDS system, there are several possible polymorphs. Between room temperature and ~1400°C, single component REDS comprising ions of erbium and smaller (e.g. erbium to lutetium along with scandium and yttrium) stabilize into a monoclinic ($C\,2/m$) phase, those comprising ions between dysprosium and gadolinium stabilize into a triclinic ($P\,\bar{1}$) phase, and those comprising europium and larger stabilize into the tetragonal ($P\,4_1$) phase.[17–19] There are additional phases that exist at elevated temperatures for many of these REDS. Only the $C\,2/m$ phase, when comprising the smallest cations (i.e. Lu, Yb, and Sc), has effectively no polymorphic transformations upon heating. This, along with favorable thermal expansion properties with respect to SiC make the $C\,2/m$ monoclinic phase (commonly denoted as the β phase or as type C as defined by Felsche[17]) technologically attractive. Despite their great promise, to date, thermal expansion and phase stability data on mixed and HE REDS remain lacking.[20]

Thermal expansion is a second-rank symmetric tensor with nine coefficients. Due to symmetry elements of the crystal, some of these coefficients are equivalent or are zero and the tensor for a monoclinic crystal with 4 distinct coefficients is shown below as Equation 2:

$$\begin{bmatrix} \alpha_{11} & 0 & \alpha_{31} \\ 0 & \alpha_{22} & 0 \\ \alpha_{31} & 0 & \alpha_{33} \end{bmatrix} \quad (2)$$

The shear coefficient (α_{13} and α_{31}) terms are equivalent due to the mirror plane present in the $C\,2/m$ structure, while the normal coefficients (α_{11}, α_{22}, and α_{33}) are all distinct. The normal tensor coefficients are orthogonal to each other and can be referred to as the principal axes only when the conditions in Equation 3 are met.

$$S_1x_1^2+S_2x_2^2+S_3\,x_3^2 = 1 \quad (3)$$

In Equation 3, S and x correspond to normal tensor coefficients and physical dimensions, respectively. In a monoclinic crystal, this condition is satisfied when S_2 is parallel to the y diad axis.[21] Previous research on the CTE of REDS has reported a linear CTE derived from dilatometry or X-ray diffraction (XRD) experiments, but tensor representations of the CTE are significantly less common.[18,20,22–28] The determination of the CTE tensor can more adequately describe anisotropy in materials than a single value in a linear CTE, or even CTE values of individual lattice parameters. With an improved representation of anisotropy, crystallographic information can be correlated to microstructural developments that impact the stress state and thermo-mechanical properties of T/EBCs. This study focuses on the phase stability of single-component, multi-component, and HE REDS and the temperature dependence of the anisotropic CTE.

2 | EXPERIMENTAL METHODS

2.1 | Powder synthesis

The REDS were synthesized via a modified sol-gel method.[29–33] Rare earth nitrates and tetraethyl orthosilicate (TEOS) served as the rare earth and silicon oxide precursors, respectively. For a REDS containing a single RE, 1.00 g of the chosen rare earth nitrate was dissolved in 30 mL of ethanol. The water content of the nitrate precursor was measured via thermogravimetric analysis (Netzsch STA-449 F1) and accounted for in the composition calculation and the mass of the rare earth nitrate was recorded to 0.001 g precision. The solution was stirred to aid in

dissolution. Separately, TEOS was measured by volume and dissolved in 30 mL of ethanol. The volume of TEOS used corresponded to a 1:1 ratio of the moles of silicon and the moles of RE in the nitrate precursor. The dissolved precursors were then combined into a single beaker containing another 30 mL of ethanol. The reaction solution was stirred and heated at 60°C and allowed to gel over 24–36 h. The gel was then placed into a platinum crucible and dried in a box furnace at 550°C for 24 h in a static air ambient. The drying process converted the sol-gel into a xerogel that was brittle but maintained the networked structure of the sol-gel.[31] The xerogel was subsequently ground into a powder with a Diamonite mortar and pestle. The powder was placed into a platinum crucible and exposed at 1400°C for 18 h in a box furnace and static air atmosphere to convert into the REDS. For a compositionally complex or high entropy REDS, the RE nitrates were dissolved together in the same solution. Equimolar quantities of each RE nitrate were batched (e.g. [Yb] = [Er] = [Y] = [Dy] for $Yb_{0.5}Er_{0.5}Y_{0.5}Dy_{0.5}Si_2O_7$). The appropriate volume of TEOS was used to keep the Si:RE ratio 1:1 with all the REs. All other synthesis steps were the same for samples containing multiple REs.

2.2 | Diffraction experiments

Preliminary XRD experiments were performed on a Panalytical Empyrean X-ray diffractometer (Cu Kα X-ray wavelength of 1.54 Å) using an Anton Parr HTK1200 N hot stage with a ramp rate of 10°C/min and temperatures from 25°C to 1200°C. Once the sample reached 50°C, the temperature was held to collect the diffraction pattern. The hold and measure profiles were repeated at subsequent 50°C intervals. Following preliminary analysis, experiments were conducted at beamline 11-ID-C at the Advanced Photon Source at Argonne National Laboratory. Transmission XRD experiments were performed on REDS powders inside of a 1 mm diameter fused quartz capillary with an X-ray energy of 105.7 keV, which corresponds to a wavelength of 0.1173 Å. A K-type thermocouple was fed in through one side of the capillary and contacted the powder to ensure that the temperature reading would report the temperature of the sample in the beam path. Diffraction patterns were collected using a Pilatus 300KW detector with a sample-to-detector distance to 1700 mm. Patterns were collected every 30 s as the sample was heated at a rate of 10°C/min from room temperature to 1000°C. This corresponded to a diffraction measurement every 5°C. Rietveld refinements were performed on the data using GSAS-II.[34] National Institute for Standards and Technology instrument standards of LaB_6 (SRM-660c and SRM-660a for lab-scale and synchrotron, respectively) and CeO_2 (SRM-674b) were used for calibration.

2.3 | Tensor analysis

Once unit cell information was extracted from the refinements, *d*-spacings were calculated and input into Coefficient of Thermal Expansion Analysis Suite (CTEAS) software to visualize the CTE tensor, acquire tensor coefficients, and calculate thermal expansion as a function of temperature.[35] The temperature range was set from 25 to 1000°C and the program fit the supplied data to a second order polynomial, and then calculated the thermal expansion and tensors through an algorithm outlined in appendix D of the CTEAS user manual.

3 | RESULTS AND DISCUSSION

3.1 | Phase mixing

The average ionic radius for the REs included in the disilicate in an 8-fold coordination were used to predict the final phase.[36] Through this model, it was hypothesized that REs could be stabilized into the *C* 2/*m* phase through a rule of mixtures as long as the average RE ionic radius was within the known range of stability as determined by Felsche.[17] For example, while $Dy_2Si_2O_7$ is not stable in the *C* 2/*m* phase, by using it as a fractional component of a REDS with other smaller radii RE ions, the average RE ionic radii is in range that is compatible with *C* 2/*m* formation. This is shown in Figure 1 where dysprosium was included in compositionally complex and high entropy mixtures. Also shown is a composition including neodymium ($Yb_{0.4}Er_{0.4}Y_{0.4}Dy_{0.4}Nd_{0.4}Si_2O_7$). For this composition the average ionic radii is 0.911 Å and this is expected to be too large to be stable in the β-phase.

The mixtures in Figure 1 were synthesized using the methods described in the experimental methods. The powders were then characterized using XRD to confirm the phases present. Figure 2 shows the XRD pattern of ytterbium disilicate produced via the method described. The powder contains majority phase peaks of monoclinic *C* 2/*m* and secondary peaks belonging to the *C* 2/*c* (X2 phase) rare-earth monosilicate line compound (i.e. Yb_2SiO_5). Analysis of peak intensities revealed that the monosilicate secondary phases were present in weight fractions of approximately 7%. This secondary monosilicate phase was present in all powders prepared in this study. Since the Si:RE was batched 1:1, the monosilicate secondary phase points towards the possible presence of an additional silica secondary phase that would

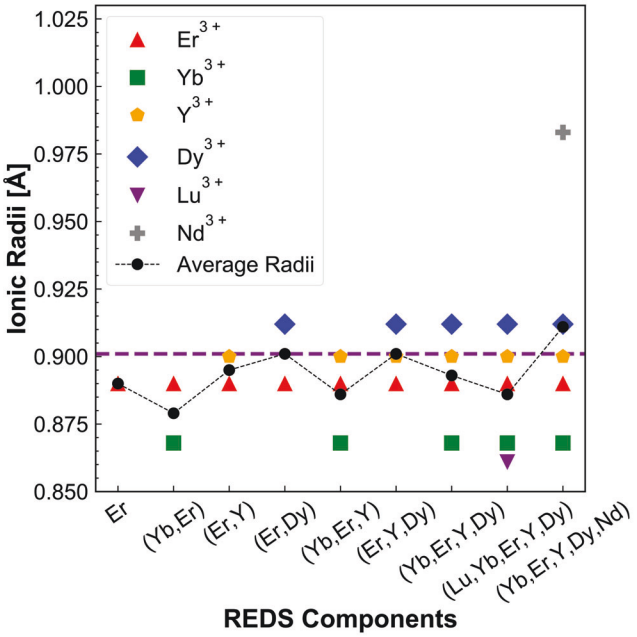

FIGURE 1 A rule of mixtures prediction of the stability of REDS in the *C* 2/*m* phase. Average ionic radii below the heavy dashed line are predicted to result in a REDS in the monoclinic *C* 2/*m* phase. Those on or above the dashed line would be the triclinic ($P\bar{1}$) phase.

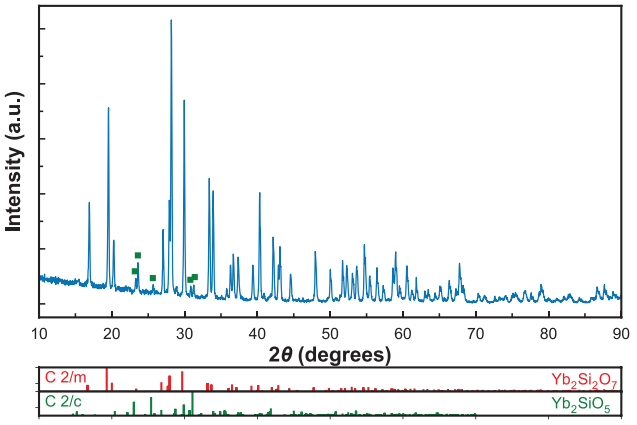

FIGURE 2 X-ray diffraction (XRD) pattern of ytterbium disilicate ($Yb_2Si_2O_7$) showing the monoclinic *C* 2/*m* phase as the primary phase with approximately 7% secondary phase presence of ytterbium monosilicate (Yb_2SiO_5). The monosilicate phase is denoted by the green squares. The reference patterns for the disilicate and monosilicate are ICSD Collection Codes 16048 and 4446 respectively.[37,38]

not appear in XRD due to difficulty in crystallizing SiO_2. The presence of the monosilicate secondary phase should not affect the composition of the primary disilicate phase since both are line compounds. Figure 3 shows XRD patterns of REDS prepared in this study. Two of the compositions, $Yb_{0.5}Er_{0.5}Y_{0.5}Dy_{0.5}Si_2O_7$ and $Lu_{0.4}Yb_{0.4}Er_{0.4}Y_{0.4}Dy_{0.4}Si_2O_7$ experimentally validate that

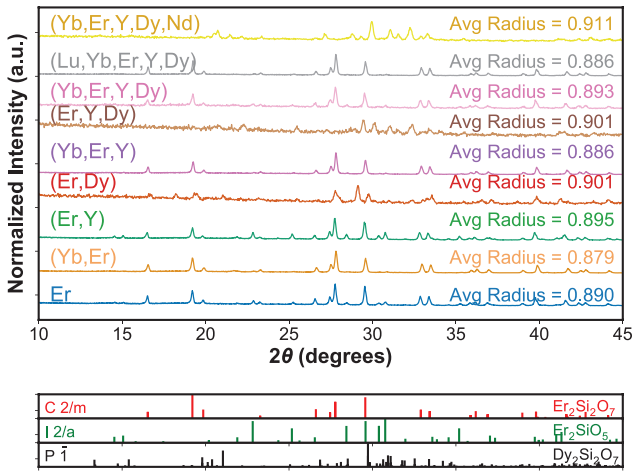

FIGURE 3 Room temperature X-ray diffraction (XRD) patterns of REDS with the labeled compositions and average RE ionic radii. Two samples contain dysprosium, both stable in the *C* 2/*m* phase. All patterns indicate stability in the *C* 2/*m* phase.

dysprosium-containing REDS can be stabilized into the *C* 2/*m* phase through a rule of mixtures. No evidence of the triclinic phase could be observed in the multi-component disilicate solid solutions comprising rare-earths with average radii below 0.900 Å. For the Nd-containing composition, however, a secondary triclinic phase was observed, demonstrating that too large of cation radii results in difficulty in stabilizing the β-phase. For the single phase compositions, variations in the β-phase peak positions are caused by differences in RE content and their distinct ionic radii leading to lattice expansion and provides an indication that solid-solutions containing each cation without phase separation or segregation of cations occurred.

3.2 | High temperature XRD

To establish the stability of these phases at elevated temperatures, high temperature XRD experiments were conducted on REDS powders with lab-scale instrumentation in a Bragg-Brentano geometry and in a transmission geometry with synchrotron radiation. All samples that were primarily β-phase and shown in Figure 3 were measured on the laboratory source, and compositions of $Yb_2Si_2O_7$, $Er_2Si_2O_7$, $(Yb,Er)_2Si_2O_7$, $(Yb,Er,Y)_2Si_2O_7$, $(Yb,Er,Y,Dy)_2Si_2O_7$, and $(Lu,Yb,Er,Y,Dy)_2Si_2O_7$ were measured at the synchrotron facility. The data taken at the beamline and with lab-scale instrumentation showed no indication of phase instability from 25 to 1000°C (1200°C for lab-scale measurements), including the REDS containing dysprosium. Contour maps of the lab-scale high temperature XRD are shown for $Er_2Si_2O_7$ and the four component $(Yb,Er,Y,Dy)_2Si_2O_7$ in Figure 4. There are no

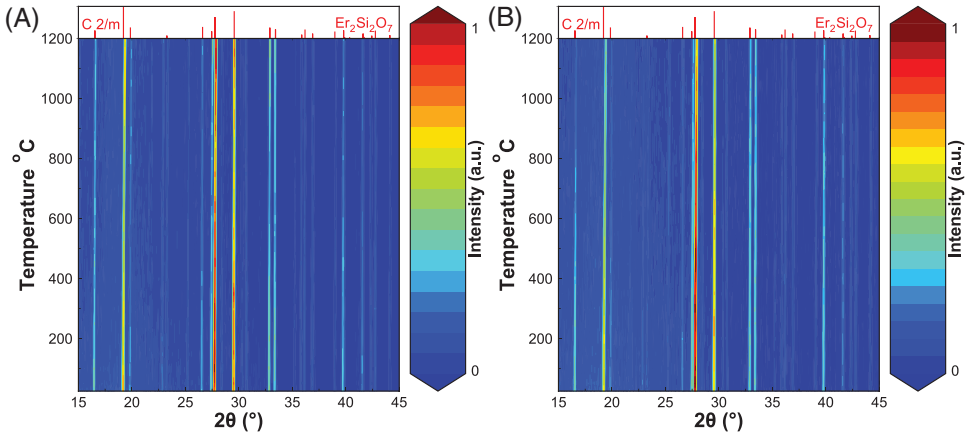

FIGURE 4 Contour maps of the high temperature X-ray diffraction (XRD) measurements on a lab-scale diffractometer for (a) $Er_2Si_2O_7$ and (b) the four component $(Yb,Er,Y,Dy)_2Si_2O_7$ disilicate. The $Er_2Si_2O_7$ reference pattern is from ICSD Collection Code 74779.[39]

new reflections that appear at higher temperatures, meaning that there are no new phases that nucleate upon heating to 1200°C detectable by XRD. Contour map XRD patterns for all other compositions from this study are available in the supplemental materials, Figure S1.

Temperature-dependent synchrotron XRD data were then refined to obtain lattice parameters, with the refinement of $Yb_2Si_2O_7$ shown in Figure 5 as an example. All data were well fit, as indicated by low weighted residual percentage (wR) values. The lattice parameters, monoclinic beta angle, and wR values are shown in Table 1. The values are reported at room temperature, 500°C, and 1000°C. The full dataset for all measured temperatures is available at the University of Virginia Dataverse.[40]

3.3 | CTE/Tensor determination

Using the CTEAS software, tensors and graphical representations of the CTE were determined. The tensor components for different compositions are given in Table 2 at 25, 500, and 1000°C. The entire dataset is available through the University of Virginia Dataverse.[40] The shear component, α_{31}, for erbium disilicate is the only coefficient that is negative at room temperature. In every other case, the shear components transition from positive to negative upon heating. The implication that this shear component has on the crystal structure will be discussed below. 3-D graphical representations of CTE are shown in Figure 6 for $Er_2Si_2O_7$ and $Yb_2Si_2O_7$ between 25 and 1000°C. The expansion along the *Y*-axis is approximate to that of the monoclinic *b*-axis unit vector direction, *X* is an arbitrary axis that is orthogonal to both *Y* and *Z*, where *Z* is approximate to the *c*-axis unit vector direction. Since the crystal is monoclinic, the angle (β) between the *a* and *c* unit vectors is not equal to 90°.

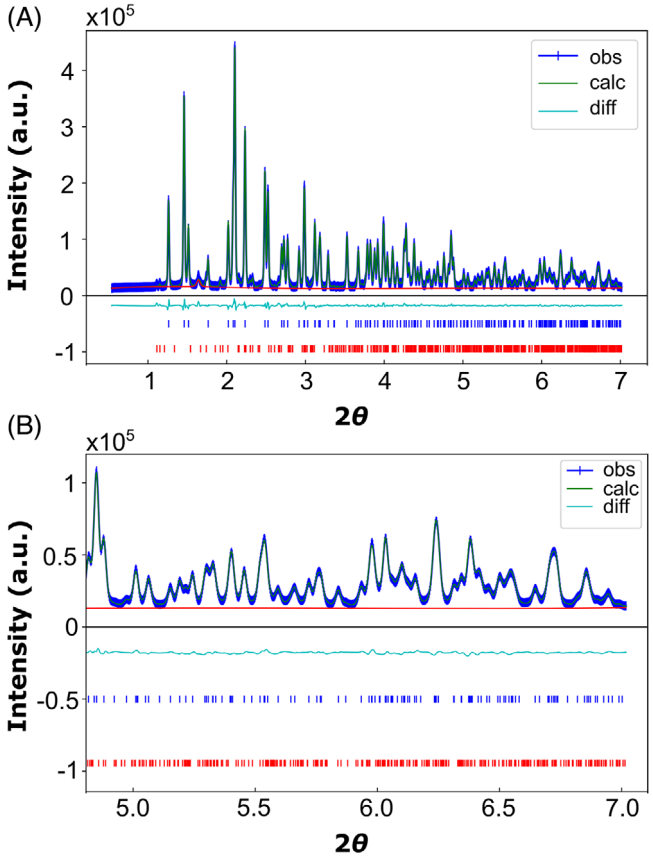

FIGURE 5 Rietveld refinement of $Yb_2Si_2O_7$ with a residual weight of approximately 3.4%. The tick marks below the fit correspond to the disilicate and monosilicate reference files (ICSD Collection Codes 16048 and 4446 respectively).[37,38] Full scan range is shown in (A), while the higher angle peaks are shown in (B). The wavelength of X-ray radiation was 0.1173 Å.

The distance from the origin to the 3-D surface corresponds to the magnitude of CTE in a specified crystallographic direction. From these expansion surface depictions, clear differences in the anisotropic thermal

TABLE 1 Lattice parameters from refined synchrotron X-ray diffraction data at 25, 500, and 1000°C. The error is an order of magnitude lower than the significant figures presented and is therefore not reported.The raw values across the entire temeprature range can be accessed through the University of Virginia Dataverse.[40] * The heating element failed during the temperature ramp and caused the heating to stop at approximately 970°C instead of 1000°C.

Composition	wR (%)	T = 25°C *a*, *b*, *c* (Å)beta (°)	T = 500°C *a*, *b*, *c* (Å)beta (°)	T = 1000°C *a*, *b*, *c* (Å)beta (°)
$Yb_2Si_2O_7$	3.313	6.80, 8.88, 4.71 101.98°	6.82, 8.89, 4.71 101.95°	6.83, 8.91, 4.72 101.98°
$Er_2Si_2O_7$	4.710	6.85, 8.94, 4.72 101.77°	6.87, 8.96, 4.72 101.78°	6.89, 8.98, 4.73 101.80°
$(Yb,Er)_2Si_2O_7$*	3.371	6.83,8.91,4.71 101.87°	6.85, 8.93, 4.72 101.86°	6.86, 8.94, 4.72 101.88°
$(Yb,Er,Y)_2Si_2O_7$	3.726	6.85, 8.94, 4.72 101.82°	6.86, 8.95, 4.72 101.82°	6.88, 8.97, 4.73 101.85°
$(Yb,Er,Y,Dy)_2Si_2O_7$	3.700	6.86, 8.95, 4.72 101.80°	6.87, 8.96, 4.72 101.79°	6.89, 8.98, 4.73 101,82°
$(Lu,Yb,Er,Y,Dy)_2Si_2O_7$*	4.023	6.85, 8.94, 4.72 101.80	6.86, 8.95, 4.72 101.80	6.88, 8.97, 4.73 101.83

TABLE 2 Rietveld refinement of synchrotron XRD data and calculated tensor components from CTEAS software. Values for all collected temperatures are publicly available through the University of Virginia Dataverse.[40] * The heating element failed during the temperature ramp and caused the heating to stop at approximately 970°C instead of 1000°C.

Composition	T = 25°C $\alpha_{11}, \alpha_{22}, \alpha_{33}, \alpha_{31}$ ($x10^{-6}°C^{-1}$)	T = 500°C $\alpha_{11}, \alpha_{22}, \alpha_{33}, \alpha_{31}$ ($x10^{-6}°C^{-1}$)	T = 1000°C $\alpha_{11}, \alpha_{22}, \alpha_{33}, \alpha_{31}$ ($x10^{-6}°C^{-1}$)
$Yb_2Si_2O_7$	3.64, 3.28, 2.43, 0.66	4.66, 3.76, 3.06, -0.17	5.74, 4.26, 3.72, -1.04
$Er_2Si_2O_7$	3.74, 3.68, 0.85, -0.29	4.73, 3.90, 1.59, -0.55	5.77, 4.12, 2.38, -0.83
$(Yb,Er)_2Si_2O_7$ *	3.41, 2.97, 1.86, 0.28	5.13, 4.04, 2.86, -0.45	6.49, 5.17, 3.93, -1.21
$(Yb,Er,Y)_2Si_2O_7$	3.42, 2.78, 1.45, 0.27	5.35, 4.06, 2.16, -0.56	7.36, 5.41, 2.91, -1.44
$(Yb,Er,Y,Dy)_2Si_2O_7$	2.43, 2.32, 0.92, 0.34	4.85, 3.79, 2.01, -0.47	7.41, 5.34, 3.17, -1.31
$(Lu,Yb,Er,Y,Dy)_2Si_2O_7$	3.09, 2.78, 1.17, 0.19	5.08, 4.00, 2.08, -0.56	7.18, 5.29, 3.04, -1.36

expansion behavior between $Er_2Si_2O_7$ and $Yb_2Si_2O_7$ can be observed. Specifically, the rotation and variations normal to the *Y* axis in the 3D surface are temperature dependent. The shift in direction of maximum CTE is illustrated more clearly in a two-dimensional representation of CTE, which is a cross-section of the 3D depictions. Figure 7 shows thermal expansion ellipsoids as polar plots in the (010) plane. The *a*- and *c*-axis direction labels correspond to crystallographic directions in the (010) plane, while distance from origin is the magnitude of CTE. The blue portions of the ellipsoid represent cooler temperatures and red indicate elevated temperatures. The minimum and maximum temperatures shown are 25°C and 1000°C, respectively, and the intermediate steps shown are in 25°C intervals. These data indicate that the principal axes are rotating upon heating. The direction of maximum CTE in $Er_2Si_2O_7$ shifts from approximately 85° to 77° relative to the *c*-axis across the range from room temperature to 1000°C. In contrast, the direction of maximum CTE shifts from approximately 113° to 67° relative to the *c*-axis from room temperature to 1000°C in $Yb_2Si_2O_7$. The angles of the eigenvectors relative to the *c*-axis were calculated via CTEAS and included in the supplemental information. The ellipsoid shift represents a shift in principal axes without the principal axes having to lie exactly at the extremum. In fact, there is a difference of a few degrees between the angle of the eigenvectors and the CTE extremes relative to the *c*-axis. Figure S2 shows the evolution of the eigenvectors (principal axes) with temperature for all compositions and illustrates that these thermal expansion extremum rotations are associated with nearly equivalent eigenvector changes. All REDS containing ytterbium exhibited a shift in direction of maximum CTE with temperature, including the high entropy sample, $(Lu,Yb,Er,Y,Dy)_2Si_2O_7$. However, as the fraction of ytterbium in the composition decreased, the degree of rotation of the principal axes was reduced compared to pure $Yb_2Si_2O_7$. While certain REs, notably ytterbium, cause a rotation in principal axes, the driving mechanism

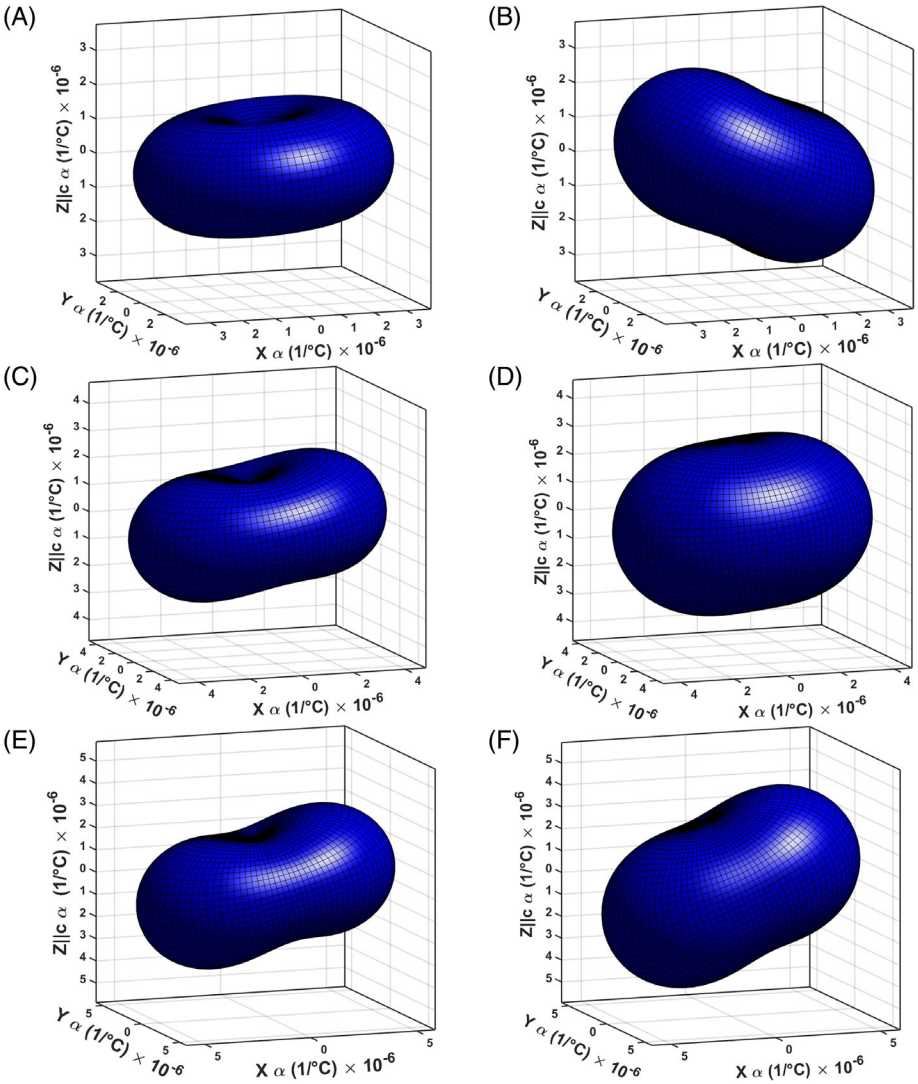

FIGURE 6 3D representations of the coefficient of thermal expansion (CTE) tensors for erbium and ytterbium disilicate at different temperatures. (A) $Er_2Si_2O_7$ at 25°C. (B) $Yb_2Si_2O_7$ at 25°C. (C) $Er_2Si_2O_7$ at 500°C. (D) $Yb_2Si_2O_7$ at 500°C. (E) $Er_2Si_2O_7$ at 1000°C. (F) $Yb_2Si_2O_7$ at 1000°C

is not clear. We speculate that this rotation is due to the ionic radii of the cations, specifically the smaller ytterbium and lutetium, filling more f-orbitals which may lead to variations in local bonding that manifests into anisotropic CTE.

This variation in bonding is speculated to only affect CTE at lower temperatures before expansion can render the influence of the f-orbitals negligible, explaining why the final crystallographic direction of the maximum CTE converges to similar final angle for all samples regardless of composition. The change in principal axes also manifests in the lattice parameters. Figure 8 shows the normalized lattice parameters and beta angles of $Er_2Si_2O_7$ and $Yb_2Si_2O_7$. The distinction between the two compositions is seen through the magnitude of the expansion in the *c*-axis lattice parameter and shape of the beta angle trend across the temperature range. For compositions that undergo a shift in principal axes, the trend in beta angle with respect to temperature can be described as a U-shape. For $Er_2Si_2O_7$, the trend in beta angle is a near constant increase with temperature and no minimum can be observed. The normalized lattice parameters and beta angles versus temperature are included in supplemental materials, Figures S3 and S4 for all other compositions. Figure 9 shows how the α_{31} component is related to the beta angle for $Yb_2Si_2O_7$. The temperature at which α_{31} transitions from negative to positive corresponds to the temperature of the beta angle minimum. The dependence of α_{31} and beta angle for all other Yb-containing compositions is shown in Figure S5.

While the use of a linear CTE is commonplace, a single value does not describe an anisotropic crystal adequately. Additionally, the thermal expansion of a lattice can vary with temperature, meaning that temperature regimes of

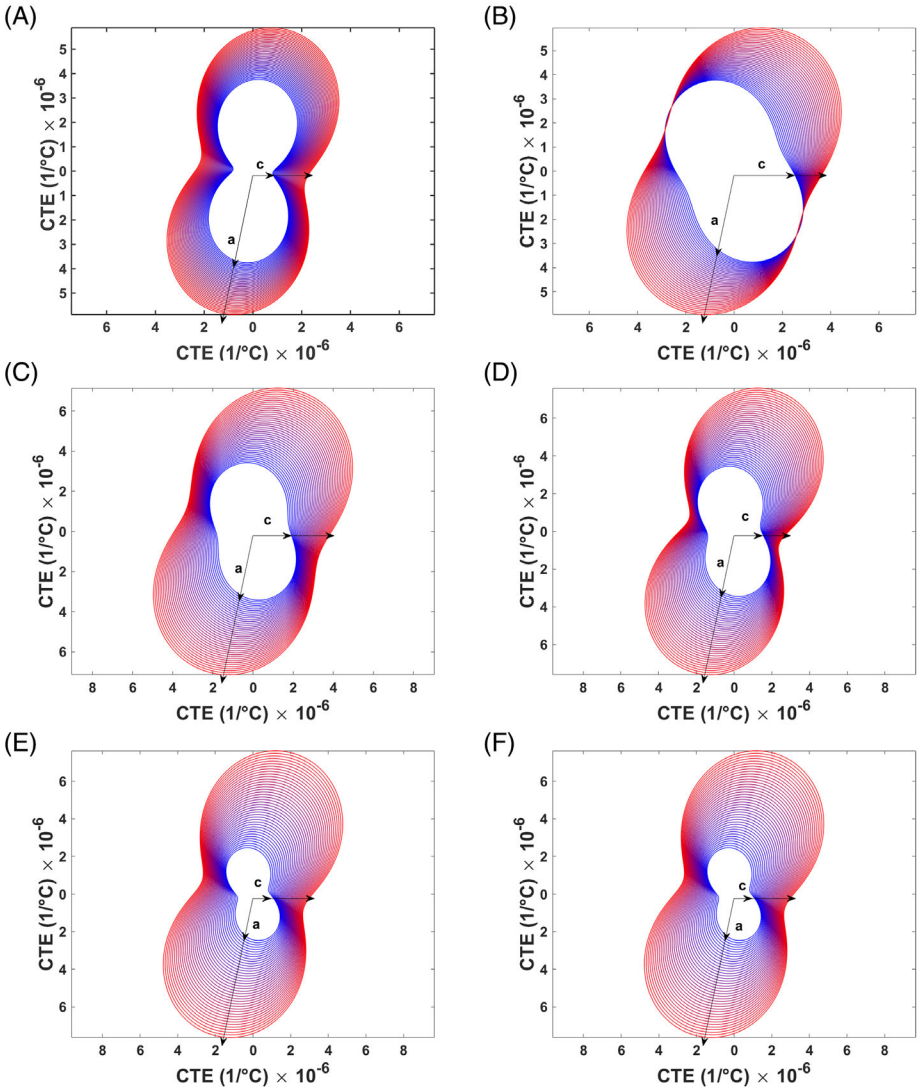

FIGURE 7 2-D polar plots showing the change in the magnitude of coefficient of thermal expansion (CTE) along crystallographic directions in the (010) plane from room temperature to 1000°C. The color gradient represents the temperature, with blue being the lowest temperature and red being the highest. The ellipsoids represent the following REDS compositions: (A) Er,DS (B) Yb,DS (C) Yb,Er DS (D) Yb,Er,Y (E) Yb,Er,Y,Dy (F) Lu,Yb,Er,Y,Dy

high and low expansion are lost within a singular linear CTE value. Linear CTE, however, is more commonly reported and is useful in comparing materials. With a tensor approach to CTE, the linear CTE can be calculated from the tensor components by averaging α_{11}, α_{22}, and α_{33}. Another method of calculating linear CTE, used by Fernández-Carrión *et al.*[20] provided similar linear CTE values without calculating tensor components. The aforementioned work by Fernández-Carrión *et al.* also reports similar linear CTE values for the REDS shown in this work.[20] The non-tensor method requires calculating $(\Delta V/3V_{RT})$, where ΔV is the change in unit cell volume relative to room temperature and V_{RT} is the unit cell volume at room temperature. Once the normalized change in unit cell volume is calculated, it is plotted versus temperature where a line of best fit is used. The slope of the line of best fit will be the estimated value of linear CTE. Both methods were assessed in this study and are shown to provide for comparable values for linear CTE. The results are provided in Table 3 for all compositions from the synchrotron diffraction experiment. Both methods of calculating the linear CTE produced values comparable to the values reported by Fernández-Carrión *et al.* for β-phase erbium and ytterbium disilicates.[20] Table 4 gives the LCTE values from several sources in literature, where ranges are reported if multiple values were found.[20,23,26,27] It is noted, however, that the tensor representation used in this work more clearly illustrates the rotation of direction of maximum thermal expansion via the change in principal axis vectors.

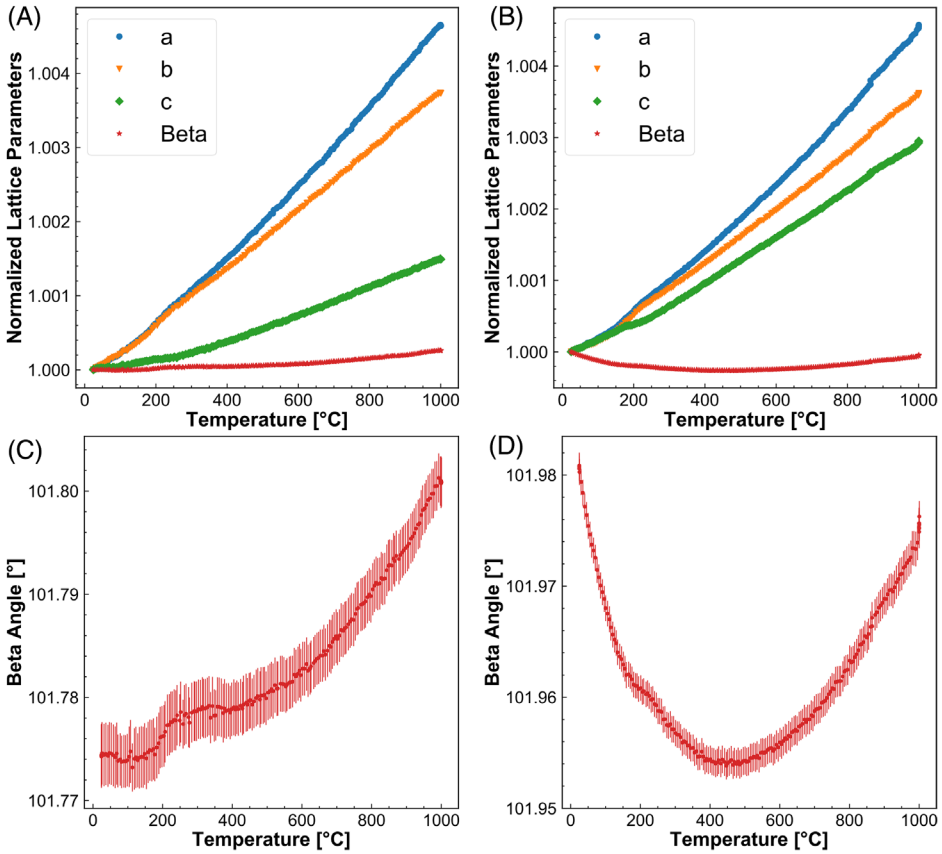

FIGURE 8 Temperature-dependent lattice parameters normalized to room temperature for (A) Er disilicate and (B)Yb disilicate showing a difference in expansion regarding the *c* unit cell direction and β angle. The difference in β angles for (C) Er disilicate and (D) Yb disilicate are shown in more detail.

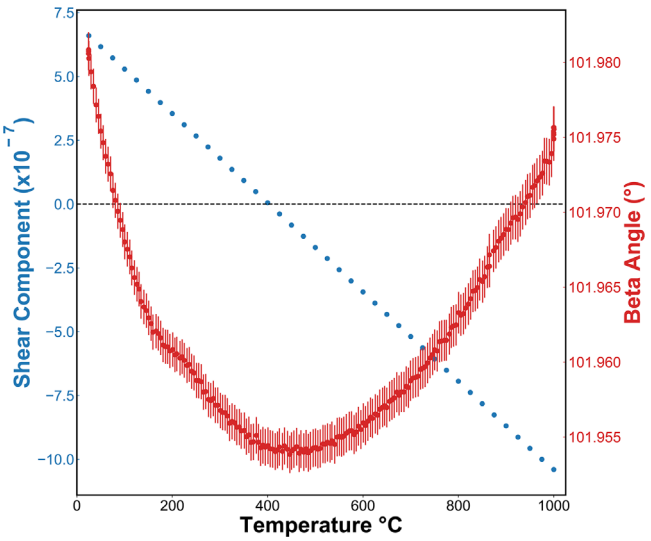

FIGURE 9 Shear component (α_{13}) and beta angle are plotted with respect to temperature for $Yb_2Si_2O_7$. A horizontal dashed line is given to represent when the shear component crosses over from positive to negative, and this intercept corresponds to similar temperatures at which the minimum of the beta curve occurs.

The temperature dependence of lattice parameters can allow for a deeper understanding of the thermo-mechanical considerations involved in engineering a T/EBC. The evolution of anisotropic CTE can impact the stress state of a polycrystalline material. It is clear from this work that ytterbium-containing compositions exhibit significant rotations in the principal axes and, therefore, complex local stresses may develop in the microstructure. Knowledge of the anisotropic CTE development, can be used to engineer T/EBCs through intentional crystallographic texturing to maximize compatibility with CMCs while minimizing the intergranular stresses that may build up through the lifetime of the material, or may require alloying with non-ytterbium elements to reduce the degree of principal axis rotation.

4 | CONCLUSION

In summary, REDS powders were prepared using a sol-gel method. Additional cations were included to create

TABLE 3 Comparison between two methods of calculating the average linear CTE from 25 to 1000°C.

Composition	LCTE: Line of Best Fit ($x10^{-6}$ 1/°C)	LCTE: Tensor Components ($x10^{-6}$ 1/°C)
$Yb_2Si_2O_7$	3.78	3.77
$Er_2Si_2O_7$	3.48	3.49
$(Yb,Er)_2Si_2O_7$	3.95	3.93
$(Yb,Er,Y)_2Si_2O_7$	3.34	3.33
$(Yb,Er,Y,Dy)_2Si_2O_7$	3.28	3.28
$(Lu,Yb,Er,Y,Dy)_2Si_2O_7$	3.58	3.56

TABLE 4 Values for single component REDS from literature and the temperature ranges for the LCTE experiments. Due to differences in experimental methods, there are variations in values relative to the LCTEs derived from the samples shown in this work, and a range is shown for REDS with multiple LCTE values found. [a]Ref. [18], [b]Ref. [20], [c]Ref. [23], [d]Ref. [26], and [e]Ref [27].

Sample	Literature LCTE ($x10^{-6}$°C^{-1})	Temperature Ranges (°C)
$Yb_2Si_2O_7$[b,c,d,e]	3.62–4.5	25–1500
$Y_2Si_2O_7$[a]	4.1	25–1400
$Er_2Si_2O_7$[b]	3.9	30–1600

single phase compositionally complex and high entropy ceramics. It was observed that the final phase of the REDS followed a rule of mixtures of cation radii that allowed for the stabilization of REs into atypical phases. The phase of the mixed and high entropy REDS studied remained stable from room temperature to 1200°C. High-temperature XRD data allowed for the determination of the second rank CTE tensors, enabling insight into anisotropy not possible with a single linear CTE value. The anisotropy of the REDS is contingent on the composition. The presence of ytterbium causes the direction of maximum CTE to shift with temperature, while $Er_2Si_2O_7$ has minimal shift in direction of maximum CTE. The influence of ytterbium in solid solution changed the principal axes and caused a distinct rotation behavior in the lattice throughout high temperature experiments. The cause for the shift in principal axes is currently unknown but is speculated to be due to the lanthanide contraction allowing for the f-orbitals of small rare-earth cations to impact bonding at lower temperature ranges. The effects of a rotating principal axis manifest through lattice parameters and CTE tensor shear components. Recognizing that these rotations exist and understanding their origins can help improve the thermomechanical considerations involved in creating T/EBCs for CMCs.

ACKNOWLEDGMENTS

The authors acknowledge Prof. Michelle Dolgos for instruction on Rietveld refinement procedures. Utilization of the Panalytical Empyrean and Anton Parr Hot-Stage instruments within UVA's Nanoscale Materials Characterization Facility (NMCF) was fundamental to this work. This work was supported by the U.S. National Science Foundation's (NSF) Designing Materials to Revolution and Engineer our Future (DMREF) Program under award number 1921973. This research used resources of the Advanced Photon Source, a U.S. Department of Energy (DOE) Office of Science user facility operated by the Office of Science by Argonne National Laboratory under Contract No. DE-AC02-06CH11357.

CONFLICT OF INTEREST

The authors declare that there is no conflict of interest that could be perceived as prejudicing the impartiality of the research reported.

ORCID

Alejandro Salanova https://orcid.org/0000-0001-7799-8612
Ian A. Brummel https://orcid.org/0000-0002-3287-6686
Elizabeth J. Opila https://orcid.org/0000-0001-5540-7084
Jon F. Ihlefeld https://orcid.org/0000-0003-0166-8136

REFERENCES

1. Lee KN, Fox DS, Bansal NP. Rare earth silicate environmental barrier coatings for SiC/SiC composites and Si_3N_4 ceramics. J Eur Ceram Soc. Jan. 2005;25(10):1705–1715. https://doi.org/10.1016/j.jeurceramsoc.2004.12.013
2. Spitsberg I, Steibel J. Thermal and environmental barrier coatings for SiC/SiC CMCs in aircraft engine applications. Int J Appl Ceram Technol. 2004;1(4):291–301.
3. Padture NP. Environmental degradation of high-temperature protective coatings for ceramic-matrix composites in gas-turbine engines. Npj Mater Degrad. Dec. 2019:3(1):11. https://doi.org/10.1038/s41529-019-0075-4
4. Padture NP. Advanced structural ceramics in aerospace propulsion. Nat Mater. Aug. 2016;15(8):804–809. https://doi.org/10.1038/nmat4687
5. Opila EJ, Smialek JL, Robinson RC, Fox DS, Jacobson NS. SiC recession caused by SiO2 scale volatility under combustion conditions: II, thermodynamics and gaseous-diffusion model. J Am Ceram Soc. 1999;82(7):1826–1834.
6. Lee KN, Fox DS, Eldridge JI, Zhu D, Robinson RC, Bansal NP, *et al*. Upper temperature limit of environmental barrier coatings based on mullite and BSAS. J Am Ceram Soc. Aug. 2003;86(8):1299–1306. https://doi.org/10.1111/j.1151-2916.2003.tb03466.x
7. Robertson AL, Solá F, Zhu D, Salem J, White KW. Microscale fracture mechanisms of HfO_2-Si environmental barrier coatings. J Eur Ceram Soc. Jul. 2019;39(7):2409–2418, https://doi.org/10.1016/j.jeurceramsoc.2019.02.001

8. Harder BJ. Oxidation performance of Si-HfO_2 environmental barrier coating bond coats deposited via plasma spray-physical vapor deposition. Surf Coat Technol. Feb. 2020;384:125311. https://doi.org/10.1016/j.surfcoat.2019.125311
9. Anton R, Leisner V, Watermeyer P, Engstler M, Schulz U. Hafnia-doped silicon bond coats manufactured by PVD for SiC/SiC CMCs. Acta Mater. Jan. 2020;183:471–483. https://doi.org/10.1016/j.actamat.2019.10.050
10. Xu Y, Hu X, Xu F, Li K. Rare earth silicate environmental barrier coatings: present status and prospective. Ceram Int. Jun. 2017;43(8):5847–5855. https://doi.org/10.1016/j.ceramint.2017.01.153
11. Cao XQ, Vassen R, Stoever D. Ceramic materials for thermal barrier coatings. J Eur Ceram Soc. Jan. 2004;24(1):1–10. https://doi.org/10.1016/S0955-2219(03)00129-8
12. Ridley M, Gaskins J, Hopkins P, Opila E. Tailoring thermal properties of multi-component rare earth monosilicates. Acta Mater. 2020;195:698–707.
13. Rost CM, Sachet E, Borman T, Moballegh A, Dickey EC, Hou D, *et al*. Entropy-stabilized oxides. Nat Commun. Dec. 2015;6(1):8485. https://doi.org/10.1038/ncomms9485
14. Miracle DB, Senkov ON. A critical review of high entropy alloys and related concepts. Acta Mater. 2017;122:448–511.
15. Zhang Y, Zuo TT, Tang Z, Gao MC, Dahmen KA, Liaw PK, *et al*. Microstructures and properties of high-entropy alloys. Prog Mater Sci. Apr. 2014;61:1–93. https://doi.org/10.1016/j.pmatsci.2013.10.001
16. Braun JL, Rost CM, Lim M, Giri A, Olson DH, Kotsonis GN, *et al*. Charge-induced disorder controls the thermal conductivity of entropy-stabilized oxides. Adv Mater. 2018;30(51):1805004.
17. Felsche J. Polymorphism and crystal data of the rare-earth disilicates of type $RE_2Si_2O_7$. J Common Met. 1970;21(1):1–14.
18. Dolan MD, Harlan B, White JS, Hall M, Misture ST, Bancheri SC, *et al*. Structures and anisotropic thermal expansion of the α, β, γ, and δ polymorphs of $Y_2Si_2O_7$. Powder Diffr, 2008;23(1):6.
19. Ridley M, Opila E. Variable thermochemical stability of $RE_2Si_2O_7$ (RE = Sc, Nd, Er, Yb, or Lu) in high-temperature high-velocity steam. J Am Ceram Soc. 2022;105(2):1330–1342. https://doi.org/10.1111/jace.18120
20. Fernández-Carrión AJ, Allix M, Becerro AI. Thermal expansion of rare-earth pyrosilicates. J Am Ceram Soc. 2013;96(7):2298–2305.
21. Nye JF. Physical properties of crystals: their representation by tensors and matrices. Oxford, UK: Oxford University Press; 1985.
22. Aparicio M, Durán A. Yttrium silicate coatings for oxidation protection of carbon–silicon carbide composites. J Am Ceram Soc. 2000;83(6):1351–1355.
23. Klemm H. Silicon nitride for high-temperature applications. J Am Ceram Soc. 2010;93(6):1501–1522.
24. Fukuda K, Matsubara H. Thermal expansion of δ-yttrium disilicate. J Am Ceram Soc. 2004;87(1):89–92.
25. Sun Z, Zhou Y, Wang J, Li M. Thermal properties and thermal shock resistance of γ-$Y_2Si_2O_7$. J Am Ceram Soc. 2008;91(8):2623–2629.
26. Ueno S, Jayaseelan DD, Kita H, Ohji T, Lin HT. Comparison of water vapor corrosion behaviors of $Ln_2Si_2O_7$ (Ln = Yb and Lu) and $ASiO_4$ (A = Ti, Zr and Hf) EBC's. in Key Eng Mater. 2006;317:557–560.
27. Chen H, Gao Y, Liu Y, Luo H. Hydrothermal synthesis of ytterbium silicate nanoparticles. Inorg Chem. 2010;49(4):1942–1946.
28. Tang X, Gao Y, Chen H, Luo H. Hydrothermal synthesis of lutetium disilicate nanoparticles. J Solid State Chem. 2012;188:38–43.
29. Galunin E, Alba MD, Vidal M. Stability of rare-earth disilicates: ionic radius effect. J Am Ceram Soc. 2011;94(5):1568–1574.
30. Parmentier J, Bodart PR, Audoin L, Massouras G, Thompson DP, Harris RK, *et al*. Phase transformations in gel-derived and mixed-powder-derived yttrium disilicate, $Y_2Si_2O_7$, by X-ray diffraction and ^{29}Si MAS NMR. J Solid State Chem. Jan. 2000;149(1):16–20. https://doi.org/10.1006/jssc.1999.8474
31. Danks AE, Hall SR, Schnepp Z. The evolution of 'sol–gel' chemistry as a technique for materials synthesis. Mater Horiz. 2016;3(2):91–112. https://doi.org/10.1039/C5MH00260E
32. Jothinathan E, Vanmeensel K, Vleugels J, Van der Biest O. Powder synthesis, processing and characterization of lanthanum silicates for SOFC application. J Alloys Compd. Apr. 2010;495(2):552–555. https://doi.org/10.1016/j.jallcom.2009.10.106
33. Feldhoff A, Arnold M, Martynczuk J, Gesing ThM, Wang H. The sol–gel synthesis of perovskites by an EDTA/citrate complexing method involves nanoscale solid state reactions. Solid State Sci. Jun. 2008;10(6):689–701. https://doi.org/10.1016/j.solidstatesciences.2007.11.030
34. Rietveld HM. A profile refinement method for nuclear and magnetic structures. J Appl Crystallogr. 1969;2(2):65–71.
35. Jones Za, Sarin P, Haggerty RP, Kriven WM. CTEAS: A graphical-user-interface-based program to determine thermal expansion from high-temperature X-ray diffraction. J Appl Crystallogr. 2013;46(2):550–553. https://doi.org/10.1107/S0021889813002938
36. Shannon RD. Revised effective ionic radii and systematic studies of interatomic distances in halides and chalcogenides. Acta Crystallogr A, 1976;32(5):751–767.
37. Smolin YI, Shepelev YF. The crystal structures of the rare earth pyrosilicates. Acta Crystallogr B, 1970;26(5):484–492.
38. Smolin YI. Crystal structure of ytterbium oxyorthosilicate Yb_2SiO_5. Sov Phys Crystallogr USSR, 1970;14(6):854.
39. Christensen AN. Investigation by the use of profile refinement of neutron powder diffraction data of the geometry of the $[Si_2O_7]^{6-}$ ions in the high temperature phases of rare earth disilicates prepared from the melt in crucible-free synthesis. Z Für Krist-Cryst Mater. 1994;209(1):7–13.
40. Salanova A, Brummel IA, Yakovenko AA, Opila BJ, Ihlefeld JF. Lattice parameters and CTE tensor components of rare earth disilicates. VA, USA: University of Virginia Dataverse; 2022. doi: 10.18130/V3/XI7QGF

SUPPORTING INFORMATION

Additional supporting information can be found online in the Supporting Information section at the end of this article.

How to cite this article: Salanova A, Brummel IA, Yakovenko AA, Opila EJ, Ihlefeld JF. Phase stability and tensorial thermal expansion properties of single to high-entropy rare-earth disilicates. J Am Ceram Soc. 2023;1–11. https://doi.org/10.1111/jace.18986